catalysts

MDPI

Article

Hierarchical Mesoporous SSZ-13 Chabazite Zeolites for Carbon Dioxide Capture

Lucy Hillen [1] and Volkan Degirmenci [1,2,*]

[1] School of Chemistry and Chemical Engineering, Queen's University Belfast, Belfast BT9 5AG, UK; lhillen02@qub.ac.uk
[2] School of Engineering, University of Warwick, Coventry CV4 7AL, UK
* Correspondence: v.degirmenci@warwick.ac.uk

Abstract: Artificial carbon dioxide capture is an alternative method to remove the carbon dioxide already accumulated in the atmosphere as well as to stop its release at its large-scale emission points at the source, such as at power plants. However, new adsorbents are needed to make the approach feasible. For this purpose, in this study, hierarchical mesoporous-microporous chabazite-type zeolites were synthesised by applying a dual-templating method. The microporous zeolite structure-directing agent N,N,N-trimethyl-1-adamantanammonium hydroxide was combined with an organosilane mesopore-generating template, 3-(trimethoxysilyl)propyl octadecyl dimethyl ammonium chloride. Materials were characterised for their structural and textural properties and tested for their carbon dioxide capture capacity both in their original sodium form and in their proton-exchanged form by means of breakthrough curve analysis and sorption isotherms. The influence of template ratios on their structure, carbon dioxide capture, and capacity have been identified. All mesoporous materials showed fast adsorption-desorption kinetics due to a reduction in the steric limitations via the introduction of a meso range network of pores. The hierarchical zeolites are recyclable with a negligible loss in crystallinity and carbon dioxide capture capacity, which makes them potential materials for larger-scale application.

Keywords: zeolite; hierarchical zeolite; mesoporous zeolite; CO_2 capture; SSZ-13; chabazite

Citation: Hillen, L.; Degirmenci, V. Hierarchical Mesoporous SSZ-13 Chabazite Zeolites for Carbon Dioxide Capture. *Catalysts* **2021**, *11*, 1355. https://doi.org/10.3390/catal11111355

Academic Editor: Francis Verpoort

Received: 26 October 2021
Accepted: 10 November 2021
Published: 12 November 2021

1. Introduction

In recent years, there has been an increasing effort to reduce levels of carbon dioxide (CO_2) emissions to the atmosphere. This CO_2 emulates from many sources, with the energy industry representing the largest share of global emissions: primarily, the combustion of fuels such as oil, natural gas, and coal [1]. There is a growing pressure for nations to take responsibility and reduce their CO_2 and other greenhouse gas emissions. Although a great increase in renewable energy generation has been achieved, the conventional coal and natural gas-fired power plants provide most of the electricity used by many countries today [2]. Developing countries with rapid industrial growth are having their intensive energy demands satisfied by burning coal and natural gas.

Current post-combustion CO_2 capture technology tends to employ amine-solvent based systems, generally using monoethanolamine (MEA) [3]. However, solid adsorbents have advantages over their liquid counterparts. They do not yield as much waste during cycling, and when spent, they can be disposable without environmental precautions. Porous materials, typically exhibiting high pore volumes and high surface areas, are considered promising choices for CO_2 capture. Carbon-based materials such as carbon nanotubes and activated carbons [4–6] along with metal–organic frameworks (MOFS) [7,8] have been extensively studied for this purpose. The adsorption capacity, selectivity, regeneration, multi-cycle durability, and adsorption/desorption kinetics are criteria commonly employed when comparing adsorbents [9,10].

In addition to post-combustion capture, the CO_2 capture systems could play an important role in the future in the net carbon zero hydrogen generation. Hydrogen is considered to be an important clean energy carrier. It can be combusted to produce power in a conventional power generation turbine and/or heat to provide heating for residential and industrial use. Moreover, hydrogen can generate electricity through a fuel cell, which could be a utilised as a lightweight system for vehicles for transportation or as a larger-scale system for districts.

The selection of suitable sorbents is a crucial matter for any capture system, and it is a complicated process because the sorbent materials must satisfy several economic and performance criteria. These criteria are brilliantly described and discussed in detail in recent reviews in the literature [11]. Fast CO_2 adsorption kinetics is essential because the kinetics controls the cycle time. To put it simply, the faster the CO_2 is adsorbed, the more economical the whole capture process will be. However, it is not the only criteria, and just fast kinetics will not make an adsorbent suitable. For instance, the easiness in regeneration needs to be considered, too. In other words, the sorbent should be regenerated by mild conditions. The regeneration is achieved by either increasing the temperature in the case of temperature swing adsorption (TSA) or by decreasing the pressure in the case of pressure swing adsorption (PSA). Therefore, the thermodynamics and kinetics affected the choice of the sorbent and the process, which is highlighted in recent literature [12,13]. Thus, the sorbent selection is a complex process involving not only the materials' characteristics but also the configuration of the reactors used [14].

In this study, we concentrated our efforts on zeolites and aimed to establish a proof of concept that the mesoporous zeolites could be considered as an option for the sorbent selection process, in particular the mesoporous SSZ-13. Zeolites have advantageous properties among other adsorbents such as their high thermal stability and tuneable pore sizes [15]. Low-silica zeolites (A, 13X, and Y) are the most common zeolites used for industrial gas separation processes [16]. However, these are very strong adsorbents and as a result can often require large temperature or pressure swings for regeneration. On the other hand, SSZ-13 is a promising alternative with the chabazite (CHA) framework that is a highly siliceous zeolite with a less hydrophilic surface due to its reduced Al content. Moreover, SSZ-13 differs from Faujasite (FAU) and LTA-type materials in that all its cation sites are accessible to interact with adsorbed molecules. Many cation sites in FAU or LTA are located within hardly accessible sodalite cages [17].

The well-defined conventional microporous SSZ-13 zeolite crystal is composed of large cages (7.3 x 12 Å) connected by eight-membered ring pore openings (3.8 x 3.8 Å), which may induce diffusional limitations when considering the dimensions of the CO_2 molecule (3.3 Å). While studies have been carried out to investigate SSZ-13 as a sorbent for CO_2 capture, these studies have been limited to microporous SSZ-13 [18]. Hudson et al. [19] reported capture capacities in the range of 3–4 $mmol \cdot g^{-1}$ for both sodium and proton analogues. Pham et al. [17] tested microporous SSZ-13 with Si/Al = 12 for CO_2 adsorption and noted that sodium and lithium forms could capture approximately 4 $mmol \cdot g^{-1}$, with potassium and proton analogues reaching adsorption capacities of 3.60 and 3.30 $mmol \cdot g^{-1}$, respectively. These values are comparable to those obtained in the literature for low-silica zeolite adsorbents [20,21], highlighting the potential of chabazite for this application.

For any new concept to succeed for CO_2 capture at power plants, it must be conceived from the beginning to operate at industrial scale. The need for a highly regenerable solid sorbent and fast sorption kinetics stems from the requirement that large amounts of the adsorbent material are required due to the large amounts of CO_2 in the flue gas [22]. In essence, this means that only processes with very short cycle times will be viable at this scale, as longer durations will lead to growing costs to meet the necessary practical efficiencies. Thus, introducing mesoporosity could provide fast adsorption/desorption kinetics alongside the desirable properties of zeolites such as their ability to work well at flue gas temperatures. There are many examples of the development of state-of-the-art mesoporous siliceous materials throughout the literature [23] with a variety of synthesis

methods and mesopore-generating tactics [24–26]. Mesoporous zeolites can be prepared by means of soft templates, which are often organosilane compounds such as octadecyl-(3-trimethoxysilylpropyl)-ammonium chloride (TPOAC) [27]. These materials act similarly to Choi's [28] bifunctional surfactant with a structure-directing ammonium head group and long alkyl chains to act as micelles in mesopore generation. This method has also been used by Chen et al. [29] in the preparation of a mesoporous LTA zeolite framework for CO_2 capture. It is demonstrated that the mesoporosity in the LTA-type zeolite enabled faster adsorption kinetics than that of its microporous counterpart, with meso-LTA reaching equilibrium within 7 min and micro-LTA continuing its uptake of CO_2 past 30 min. The mesoporous zeolite was able to capture 3.08 $mmol \cdot g^{-1}$ CO_2—a value comparable with other solids in the literature. Similarly, chabazite (CHA) framework type SSZ-13 materials can be synthesised by a dual-templating method [30,31]. In this method, mesoporous SSZ-13 was obtained by using N,N,N-trimethyl-1-adamantanammonium hydroxide (TMAdOH) as the structure-directing agent and $C_{22}H_{45}–N^+(CH_3)_2–(CH_2)_4–N^+(CH_3)_2–C_4H_9Br_2$ ($C_{22\text{-}4\text{-}4}Br_2$) as the mesopogen. It was shown that the mesoporous zeolite contains a three-dimensional assembly of small nanocrystals.

We synthesized a series of microporous and mesoporous CHA-type zeolites in their parent sodium (Na^+) and proton (H^+)-exchanged forms, with an Si/Al ratio of either 20 or 40. A degree of mesoporosity introduced with the use of a mesopore-generating template (mesopogen)–3-(trimethoxysilyl)propyl octadecyl dimethyl ammonium chloride—concurrently with the conventional structure-directing agent (SDA) N,N,N-trimethyl-1-adamantanammonium hydroxide—during synthesis in molar mesopogen to SDA ratios of 0.2, 0.4, 0.6, and 0.8. Materials were characterised by X-ray diffraction (XRD), N_2 adsorption at 77 K, and scanning electron microscopy (SEM). Materials were tested for their CO_2 adsorption; the adsorption capacity and rates of intake were calculated and compared. In this study, we used a combination of CO_2 isotherms and breakthrough curves, which allowed for a simple and effective method of comparing the kinetics and sorption performance of the materials under study. We observed that mesoporous materials showed faster adsorption/desorption kinetics than their microporous counterparts. It is inferred that this is due to the introduction of a network of a meso-scale range of pores, which reduces diffusion pathways. The hierarchical mesoporous zeolites were found to be recyclable, and their carbon dioxide capture capacity is retained, which proves their potential for large-scale application.

2. Results and Discussion

2.1. Characterisation of Materials

The XRD patterns of SSZ-13 samples (Figure 1) can be seen to exhibit characteristic peaks at 9.40°, 20.45°, and 30.40°, which are directly comparable to the IZA database obtained data for Chabazite-type materials. Upon ion exchange of Na-SSZ-13 to H-SSZ-13, there was no discernible change in the peaks. The intense peaks observed both in H-SSZ-13 and Na-SSZ-13 samples indicate highly crystalline materials. The full width half maximum (FWHM) defines the sharpness of the peaks, and it is a measure of the crystallinity of solids in powder XRD analysis. The sharp peaks indicate high crystallinity, whereas broader peaks are an indication of lesser crystallinity. The FWHM of the main peak at 10° is given in Table 1 for the materials. It is seen that the values for mesoporous materials are similar to those of the conventional microporous materials. This proves that the conventional highly crystalline microporous zeolites and the mesoporous materials have comparable crystallinity.

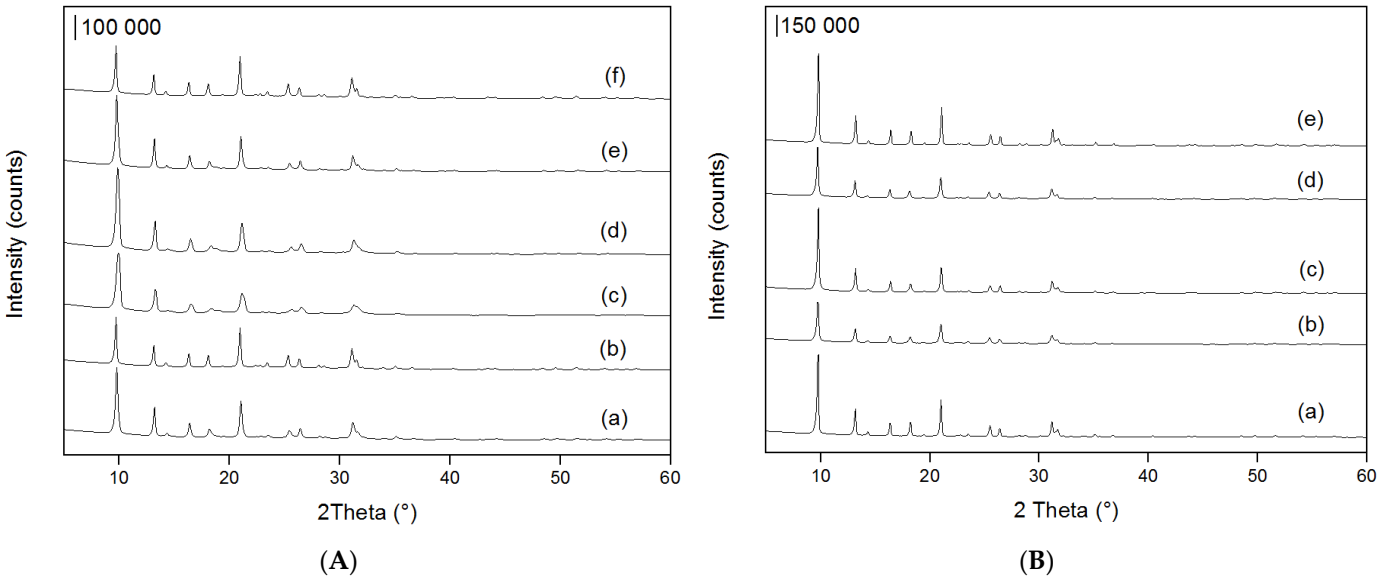

Figure 1. (**A**) XRD patterns of (a) Na-SSZ-13-micro-20, (b) Na-SSZ-13-micro-40, (c) Na-SSZ-13-meso-0.2, (d) Na-SSZ-13-meso-0.4, (e) Na-SSZ-13-meso-0.6, and (f) Na-SSZ-13-meso-0.8; and (**B**) XRD patterns of (a) H-SSZ-13-micro-20, (b) H-SSZ-13-micro-40, (c) H-SSZ-13-meso-0.2, (d) H-SSZ-13-meso-0.4, and (e) H-SSZ-13-meso-0.6.

Table 1. The crystallinity of the conventional microporous and hierarchical mesoporous zeolites in Na^+ and H^+ forms.

Material	FWHM [1]	Material	FWHM [1]
Na-SSZ-13-micro-20	0.25	H-SSZ-13-micro-20	0.19
Na-SSZ-13-micro-40	0.18	H-SSZ-13-micro-40	0.23
Na-SSZ-13-meso-0.2	0.42	H-SSZ-13-meso-0.2	0.18
Na-SSZ-13-meso-0.4	0.33	H-SSZ-13-meso-0.4	0.20
Na-SSZ-13-meso-0.6	0.26	H-SSZ-13-meso-0.6	0.17
Na-SSZ-13-meso-0.8	0.19	-	-

[1] Full width half maximum of the main peak.

SEM images of materials (Figure 2) suggest that SSZ-13 shows crystals, ranging from small crystals of roughly 1 µm in size to larger crystals of 3 to 4 µm in size. The microporous analogues exhibit the most defined crystals in both Na^+ and H^+ forms, while a degree of amorphous material can be seen around the zeolite crystals in many instances. Nevertheless, within the XRD patterns, the absence of a broad peak around 30° 2 Theta associated with amorphous silica suggests that this is not sufficient to have a detrimental effect on the crystallinity of the materials.

Figure 3a–d shows the N_2 sorption isotherms of mesoporous Na-SSZ-13-meso samples. They all exhibit type 4 hysteresis, indicating the presence of mesopores. This is confirmed by examination of the pore size distribution curves in Figure 4A. A template ratio of 0.2 shows a narrow distribution of small mesopores (roughly 40 Å) and a broad distribution of larger mesopores (100–200 Å). Increasing the template ratio to 0.4 maintains the narrow distribution of small mesopores and shows a lesser contribution to porosity from the broadly distributed 100–200 Å mesopores. Increasing this ratio further to 0.6 shows the loss of larger mesopores from the material and is illustrative of a higher degree of microporous material. The Na-SSZ-13-meso materials synthesized using the highest template ratio of 0.8 resulted in an irregular distribution of small and large mesopores, indicating that it is most likely beyond the ideal synthesis conditions. The N_2 sorption results for H-SSZ-13-meso are shown in Figures 3e–g and 4B. Materials synthesized with template ratios of 0.2 and 0.4 can be seen to exhibit type 4 hysteresis, which is indicative of their mesoporous nature. This is confirmed by the pore size distribution curves, which indicate that the 0.2 material

has a narrow distribution of small mesopores and a broad distribution of larger mesopores. An increase in the template ratio to 0.4 leads to a small contribution of small mesopores and a substantial increase in larger mesopores. H-SSZ-13-meso-0.6 appears to lose much of its mesoporous nature but maintains its microporous structure, as seen again in Figure 3g by the N_2 sorption type 1 isotherm. This is highlighted by the decrease in mesopore volume from 0.125 to 0.035 $cm^3 \cdot g^{-1}$. H-SSZ-13-meso samples have slightly larger total pore volumes than Na-SSZ-13-meso samples.

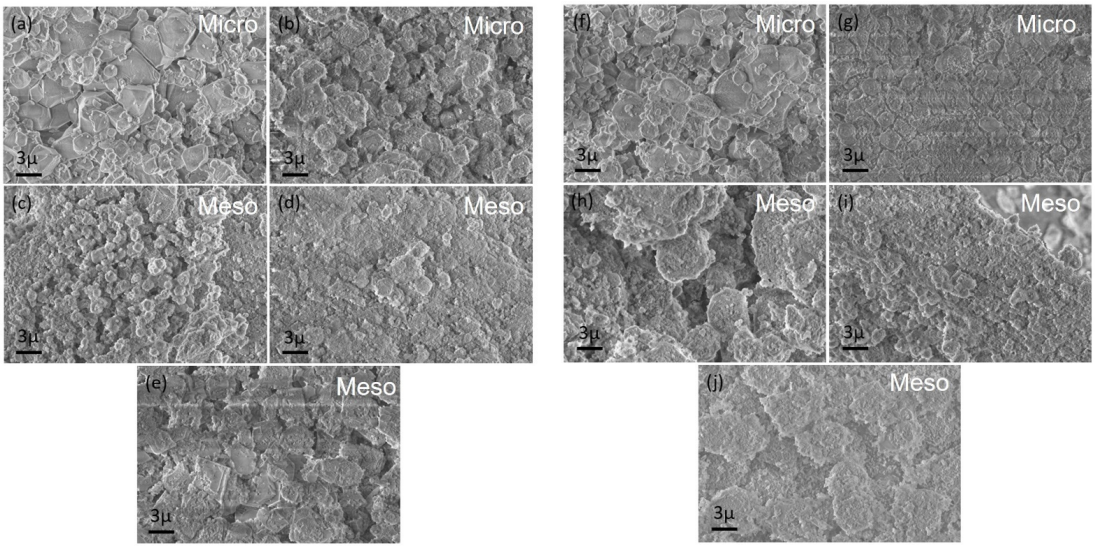

Figure 2. (**A**) SEM images of (a) Na-SSZ-13-micro-20, (b) Na-SSZ-13-micro-40, (c) Na-SSZ-13-meso-0.2, (d) Na-SSZ-13-meso-0.4, and (e) Na-SSZ-13-meso-0.6; and (**B**) SEM images of (f) H-SSZ-13-micro-20, (g) H-SSZ-13-micro-40, (h) H-SSZ-13-meso-0.2, (i) H-SSZ-13-meso-0.4, and (j) H-SSZ-13-meso-0.6.

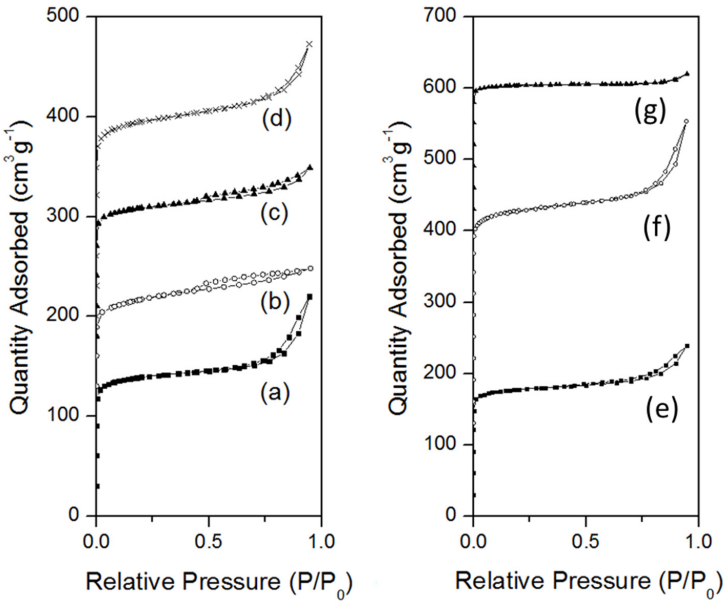

Figure 3. N_2 sorption on (a) Na-SSZ-13-meso-0.2, (b) Na-SSZ-13-meso-0.4, (c) Na-SSZ-13-meso-0.6, (d) Na-SSZ-13-meso-0.8, (e) H-SSZ-13-meso-0.2, (f) H-SSZ-13-meso-0.4, (g) H-SSZ-13-meso-0.6. Isotherms are vertically offset by 100 $cm^3 g^{-1}$.

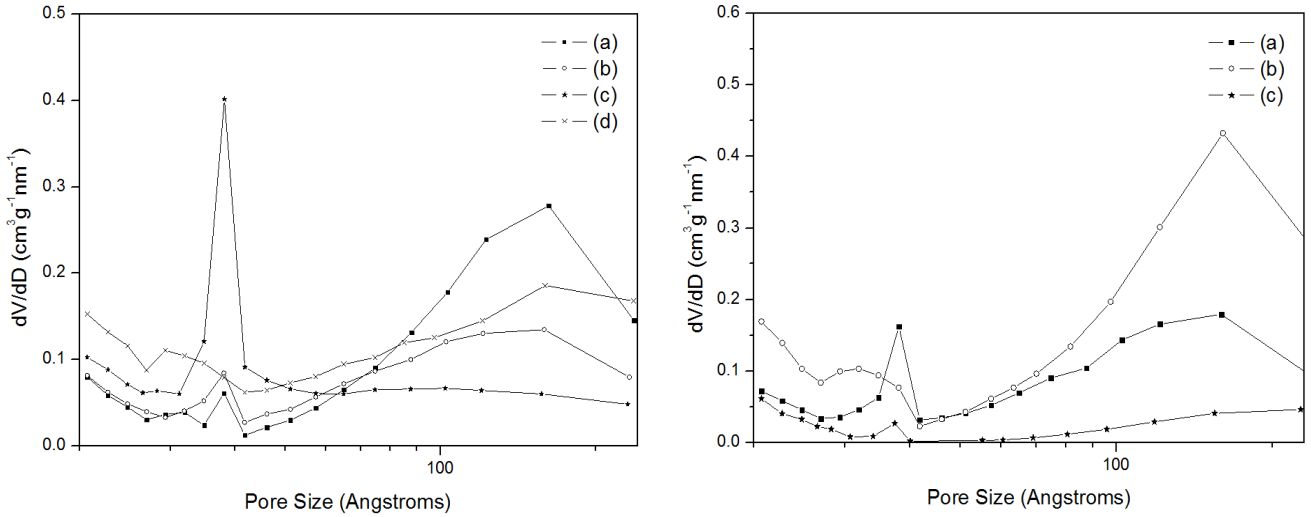

Figure 4. (**A**) Pore size distribution of (a) Na-SSZ-13-meso-0.2, (b) Na-SSZ-13-meso-0.4, (c) Na-SSZ-13-meso-0.6, and (d) Na-SSZ-13-meso-0.8; and (**B**) (a) H-SSZ-13-meso-0.2, (b) H-SSZ-13-meso-0.4, and (c) H-SSZ-13-meso-0.6. X-axis scale is Log_{10}.

The BET data as shown in Table 2 indicate that purely microporous Na-SSZ-13-micro possesses no mesopore volume, while all the mesoporous samples show mesoporosity. A mesopore volume of 0.157 $cm^3 \cdot g^{-1}$ is observed in Na-SSZ-13-meso-0.2, and this decreases to 0.105 and 0.097 $cm^3 \cdot g^{-1}$ in Na-SSZ-13-meso-0.4 and Na-SSZ-13-meso-0.6, respectively. This is most likely due to a reduction in the broad distribution of larger mesopores present in Na-SSZ-13-meso-0.2. The lowest mesopore volume is seen in Na-SSZ-13-meso-0.6. This material possesses the uniform small mesopores, which will inevitably not contribute as much to the cumulative mesopore volume as their larger counterparts. Mesopore volume increases after an increase in template ratio from 0.6 to 0.8 due to the loss of uniform pore size distribution and indicates an irregular distribution of large mesopores. It can be speculated that template ratios of 0.2 and 0.4 may lead to the formation of thin zeolite sheets with significant mesopores. Increasing the template ratio to 0.6 may lead to a phase separation between the mesoporgen and the SDA templates. This may lead to a deficiency of integration of the mesoporgen, and the zeolite crystals being formed consequently result in mainly a microporous structure. A further increase in the template ratio to 0.8 likely prompted Si–O–Si formation, resulting in a mesoporous silica-type material around the zeolite crystals.

Table 2. Nitrogen physisorption results.

Material	BET Surface Area (m^2g^{-1})	Micropore Volume (cm^3g^{-1})	Mesopore Volume (cm^3g^{-1})	Total Pore Volume (cm^3g^{-1})
Na-SSZ-13-micro-20	594	0.246	-	0.246
Na-SSZ-13-meso-0.2	497	0.177	0.157	0.334
Na-SSZ-13-meso-0.4	498	0.181	0.105	0.286
Na-SSZ-13-meso-0.6	567	0.204	0.097	0.301
Na-SSZ-13-meso-0.8	807	-	0.165	0.165
H-SSZ-13-micro-40	679	0.282	-	0.230
H-SSZ-13-meso-0.2	636	0.240	0.125	0.365
H-SSZ-13-meso-0.4	655	0.251	0.142	0.393
H-SSZ-13-meso-0.6	735	0.298	0.035	0.333

2.2. Breakthrough Curves

Chabazite type SSZ-13 materials have been tested for their CO_2 capture by means of both breakthrough experiments and CO_2 isotherms. Figure 5 shows the breakthrough curves for microporous zeolites in sodium and proton forms: Na-SSZ-13-micro-40 and H-SSZ-13-micro-40 with noticeably different shapes. Na-SSZ-13-micro is seen to have a breakthrough time of five minutes and becomes fully saturated after 15 min of CO_2 exposure. In contrast, adsorption occurs rapidly in H-SSZ-13-micro-40, breaking through immediately and reaching complete saturation in less than 10 min. Similarly, full desorption in H-SSZ-13-micro-40 takes 10 min, and this leads to a more rapid sorption cycle than that of Na-SSZ-13-micro-40. This is clearly visible when the five consecutive sorption cycles of both materials are compared. The five consecutive sorption cycles of H-SSZ-13-micro-40 takes approximately the same time as three consecutive Na-SSZ-13-micro-40 cycles.

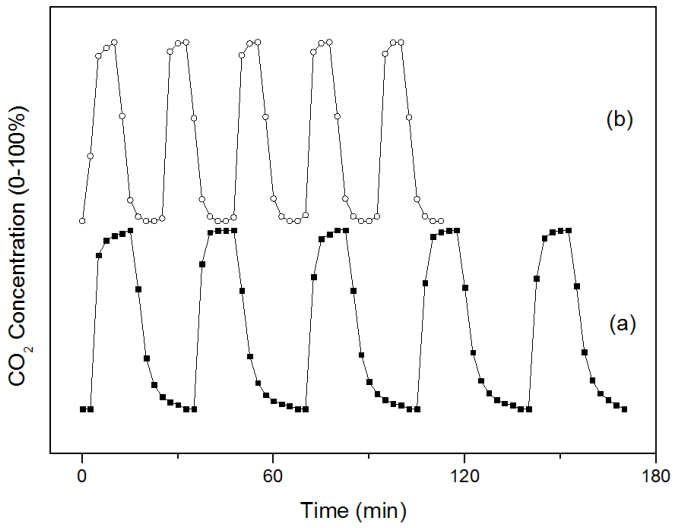

Figure 5. Five consecutive CO_2 adsorption/desorption cycles on (a) Na-SSZ-13-micro-40 and (b) H-SSZ-13-micro-40 materials.

The adsorption/desorption cycles of mesoporous Na-SSZ-13-40 materials synthesized with the template ratios of 0.2, 0.4, 0.6, and 0.8 are shown in Figure 6 A. These are compared to the sorption cycles of the microporous Na-SSZ-13-40 material on the same plot. It is seen that all Na-SSZ-13-meso samples exhibit faster sorption kinetics than the Na-SSZ-13-micro material. Mesoporous materials have breakthrough times between 2.5 and 5 min except for Na-SSZ-13-meso-0.2, which breaks through immediately. Na-SSZ-13-meso-0.6 has the slowest kinetics of the four, and this is most likely due to its comparatively lower mesopore volume. A narrow distribution of mesopores (d ~ 5.13 nm) is observed in Na-SSZ-13-meso-0.6. The larger pore volumes that the other materials show could decrease the diffusional limitations, which may allow the observed faster CO_2 sorption kinetics. A similar pattern can be seen in proton-exchanged samples (Figure 6B) in that all mesoporous samples have faster sorption kinetics than the microporous H-SSZ-13-micro material.

2.3. CO_2 Adsorption Isotherms

CO_2 capacity was determined via the measurements of CO_2 isotherms of the materials, as shown in Figure 7, where the CO_2 adsorption capacity and the adsorption rate together with the Langmuir isotherm parameters are tabulated in Table 3. Microporous Na-SSZ-13-micro exhibits reasonable capacities of 3.23 and 3.18 $mmol \cdot g^{-1}$ for Si/Al ratios of 20 and 40 respectively, and this capacity is reduced with the introduction of different degrees of mesoporosity, with a capacity of 2.63 $mmol \cdot g^{-1}$ for a template ratio of 0.2 as being the lowest. Increasing the mesoporgen to SDA template ratio leads to a rise in capacity. A template ratio of 0.6 results in the greatest capacity observed among the Na-SSZ-13-meso

analogues. The value of 3.10 mmol·g^{-1} is similar to those of the microporous materials. This agrees with the N_2 physisorption results because Na-SSZ-13-0.6 is more microporous. The increase in the mesoporgen to SDA template ratio leads to a rise in CO_2 capacity, which coincides with the increase in micropore volume. This implies that the higher amount of mesoporgen in the synthesis solution prevents it from being involved in the structure formation, and materials tend to become more microcrystalline. Therefore, there is an optimum template ratio.

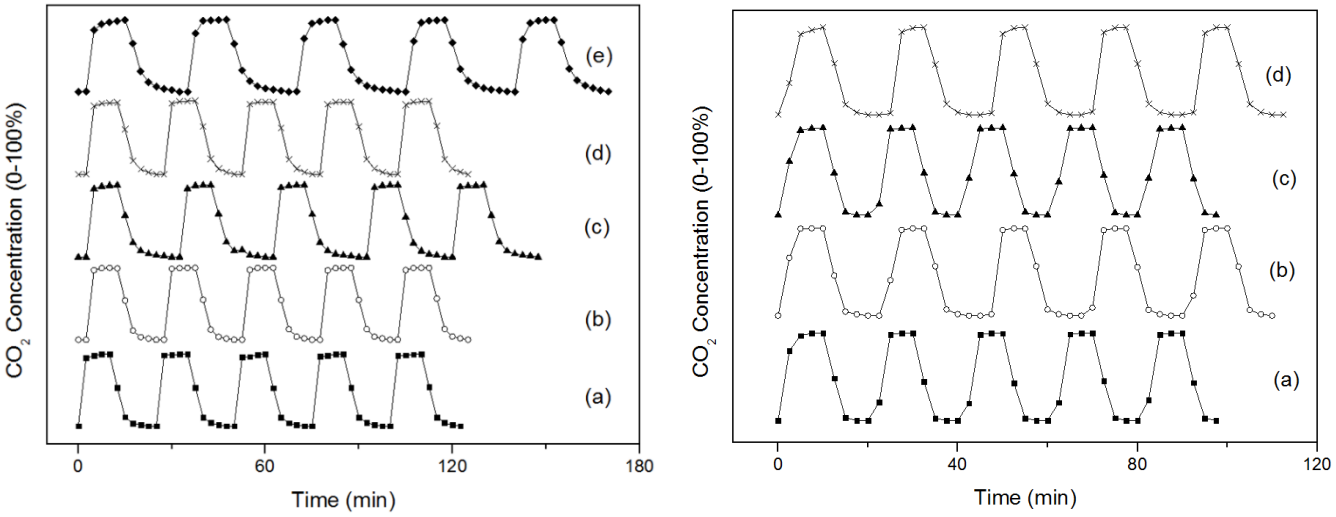

(**A**) (**B**)

Figure 6. (**A**) The CO_2 adsorption/desorption cycles of (a) Na-SSZ-13-meso-0.2, (b) Na-SSZ-13-meso-0.4, (c) Na-SSZ-13-meso-0.6, (d) Na-SSZ-13-meso-0.8, and (e) Na-SSZ-13-micro; (**B**) CO_2 adsorption cycles of (a) H-SSZ-13-meso-0.2, (b) H-SSZ-13-meso-0.4, (c) H-SSZ-13-meso-0.6, and (d) H-SSZ-13-micro.

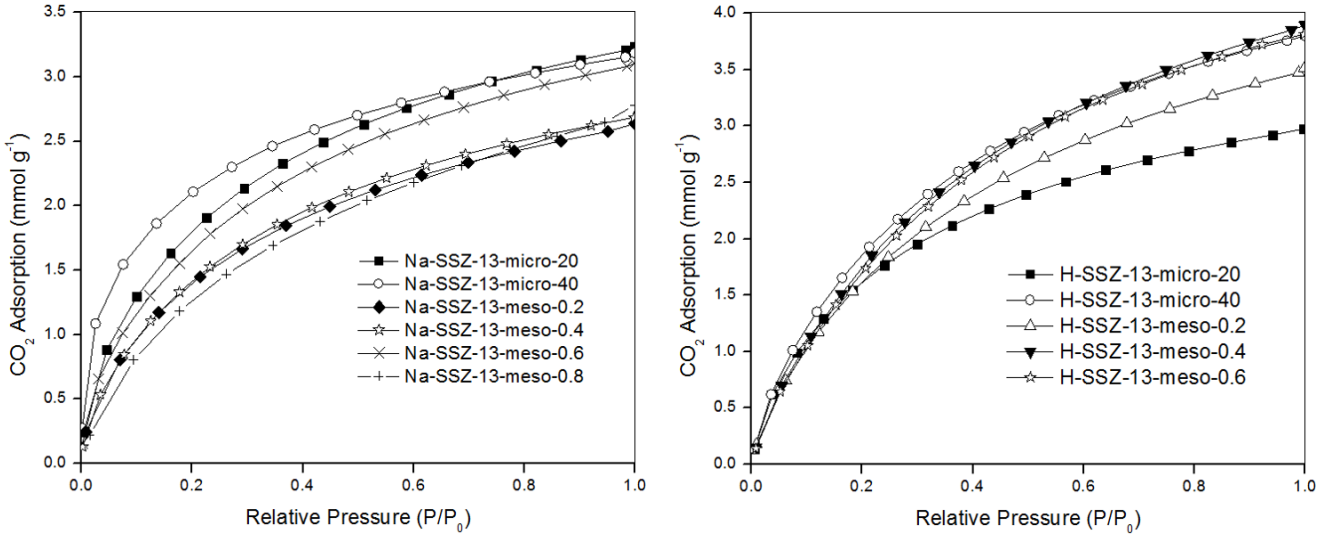

(**A**) (**B**)

Figure 7. (**A**) CO_2 adsorption isotherms for Na-SSZ-13 materials; (**B**) CO_2 adsorption isotherms for H-SSZ-13 materials.

Table 3. CO_2 adsorption capacity and rate and the Langmuir isotherm parameters for microporous and mesoporous materials.

Material	K	V_{max} (cm^3g^{-1})	R^2	CO_2 Capacity ($mmol \cdot g^{-1}$)	CO_2 Adsorption Rate ($mmol \cdot g^{-1}min^{-1}$)
Na-SSZ-13-micro-20	17.95	72.56	0.9920	3.23	0.13
Na-SSZ-13-micro-40	13.28	71.36	0.9922	3.18	0.11
Na-SSZ-13-meso-0.2	15.77	59.05	0.9945	2.63	0.18
Na-SSZ-13-meso-0.4	15.28	60.13	0.9850	2.68	0.22
Na-SSZ-13-meso-0.6	16.98	69.52	0.9800	3.10	0.16
Na-SSZ-13-meso-0.8	18.72	62.33	0.9868	2.78	0.19
H-SSZ-13-micro-20	23.14	85.15	0.9818	3.80	0.22
H-SSZ-13-micro-40	17.02	66.64	0.9912	2.97	0.17
H-SSZ-13-meso-0.2	23.40	78.65	0.9881	3.51	0.28
H-SSZ-13-meso-0.4	26.35	87.29	0.9857	3.90	0.26
H-SSZ-13-meso-0.6	25.87	85.47	0.9843	3.52	0.28

The introduction of mesoporosity in zeolites in Na form leads to an increase in adsorption rate. The fastest is the Na-SSZ-13-meso-0.4 material, which has high mesoporosity. Na-SSZ-13-meso-0.6 has the slowest adsorption rate out of the mesoporous materials in Na form. This could be caused by the fact that mesopores in this material are predominantly in the 40 Å pore size range (Figure 4A). In contrast, the other mesoporous materials have a broader pore size distribution covering the 100–200 Å pore size range (Figure 4). Hence, the material possesses more diffusional hindrances and behaves similarly to the microporous materials. Na-SSZ-13-meso-0.4 has a more significant contribution from mesopores of larger pore size, facilitating the fastest sorption kinetics and thus the greatest rate of CO_2 uptake. Multiple solid sorbents have been reported in the literature, and their capacity is tabulated in reviews [32–34]. The adsorption capacity of Na-SSZ-13 mesoporous zeolites range between 2.63 and 3.10 $mmol \cdot g^{-1}$, whereas the H-SSZ-13 mesoporous zeolites are in between 3.51 and 3.90 $mmol \cdot g^{-1}$. The capacity of carbonaceous solid sorbents including multiple variants of activated carbon, graphene, and carbon molecular sieves are 0.57–3.32 $mmol \cdot g^{-1}$. On the other hand, conventional microporous zeolites including 13X, NaX, NaY, 4A, ZSM-5, and mordenite show capacities of 1.13–5.71 $mmol \cdot g^{-1}$. MOFs usually have higher CO_2 capacities ranging from 1.48 to 33.5 $mmol \cdot g^{-1}$. In this respect, the CO_2 capacity of mesoporous SSZ-13 materials lie somewhere in the middle of the range, which is similar to most other zeolites. The comparison of the rate of adsorption of mesoporous zeolites with their conventional microporous counterparts reveals that the mesoporous zeolites are slightly faster. The mesoporous zeolites show a range of rates at 0.18–0.28 $mmol \cdot g^{-1}min^{-1}$, whereas the microporous zeolite CO_2 adsorption rates are slightly slower in between 0.11 and 0.22 $mmol \cdot g^{-1}min^{-1}$ (Table 3). Therefore, the mesoporous SSZ-13 zeolites render more promising kinetics than conventional microporous SSZ-13 zeolites.

When the proton forms of zeolites (H-SSZ-13-meso) are compared, it is seen that the mesoporous materials exhibit a faster rate of adsorption than their microporous analogues (Figure 8). The adsorption rates of mesoporous zeolites in proton form are relatively similar to each other, but the faster ones are H-SSZ-13-meso-0.2 and H-SSZ-13-meso-0.6, both of which have almost equal capacity: 3.51 and 3.52 $mmol \cdot g^{-1}$. H-SSZ-13-meso-0.6 is primarily a microporous material, since it has a low mesopore volume but consists of a considerable micropore volume. It can be concluded that the optimum template ratio is 0.2 among the mesoporous zeolites in proton form.

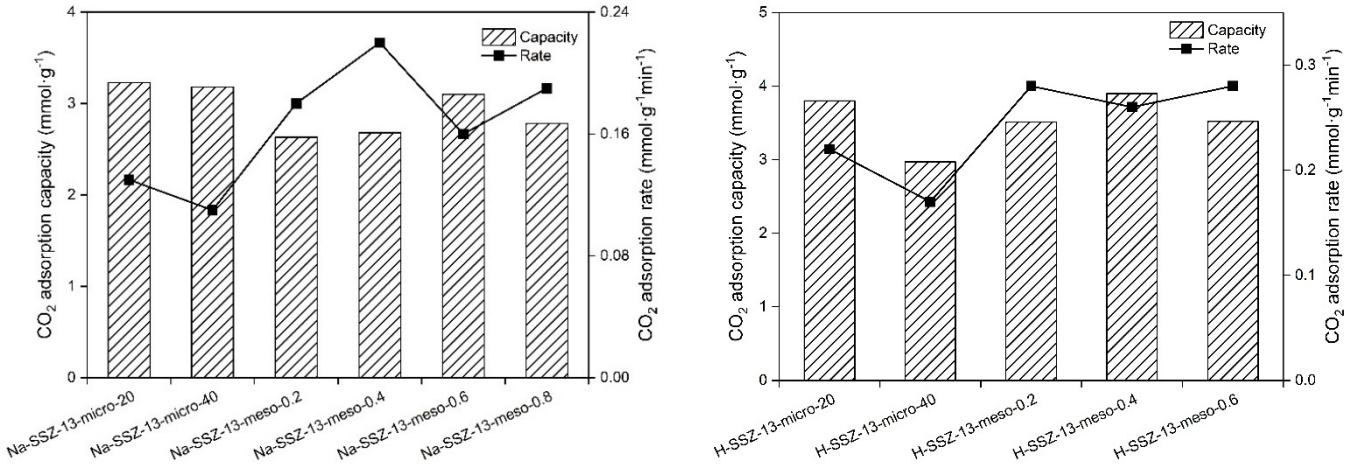

(**A**) (**B**)

Figure 8. CO_2 adsorption capacity and adsorption rate in (**A**) Na-SSZ-13 materials; (**B**) H-SSZ-13 materials.

It is apparent that the microporous materials, while possessing a higher CO_2 capacity, have a slower rate of adsorption when compared to mesoporous samples due to their steric limitations. It can be concluded that optimum sorption kinetics in both Na and H ion forms of SSZ-13 exist when there is a presence of both small and large pore diameter mesopores. This is the case in both of the best-performing samples: Na-SSZ-13-meso-0.4 and H-SSZ-13-meso-0.2. This combination seems to allow for a reduction in the steric and diffusional limitations of CO_2 molecules through the 3.8 × 3.8 Å channels of the zeolites while still maintaining a highly crystalline structure. Overall, it is observed that H-SSZ-13 materials have generally higher capacities than Na-SSZ-13. From the N_2 sorption data, it is also shown that H-SSZ-13 samples possess slightly larger pore volumes than Na-SSZ-13, which is likely due to the size of the Na^+ ions within the zeolite cages. It is probable that this is leading to the higher CO_2 capacities for the proton analogues. Pham et al. [17] discussed that the comparatively lower ionic radius of H^+ also leads to a much lower heat of adsorption, and this is in line with the results obtained in this study, with H-SSZ-13 being easily and quickly regenerable alongside superior rates of adsorption.

2.4. Stability of Materials

Recyclability is an essential property that an ideal adsorbent for CO_2 must possess. Na-SSZ-13-meso-0.4 was subjected to adsorption/desorption cycles over 240 min. It is seen that there was not any noticeable decrease in the sorption capacity over this period, as shown in Figure 9A, and the XRD patterns indicated a high degree of crystallinity, as shown in Figure 9B. H-SSZ-13 being easily and quickly regenerable alongside with its stability makes it a promising material in real-life application. A follow-up study on a larger scale and long-term operation could prove the applicability of this material.

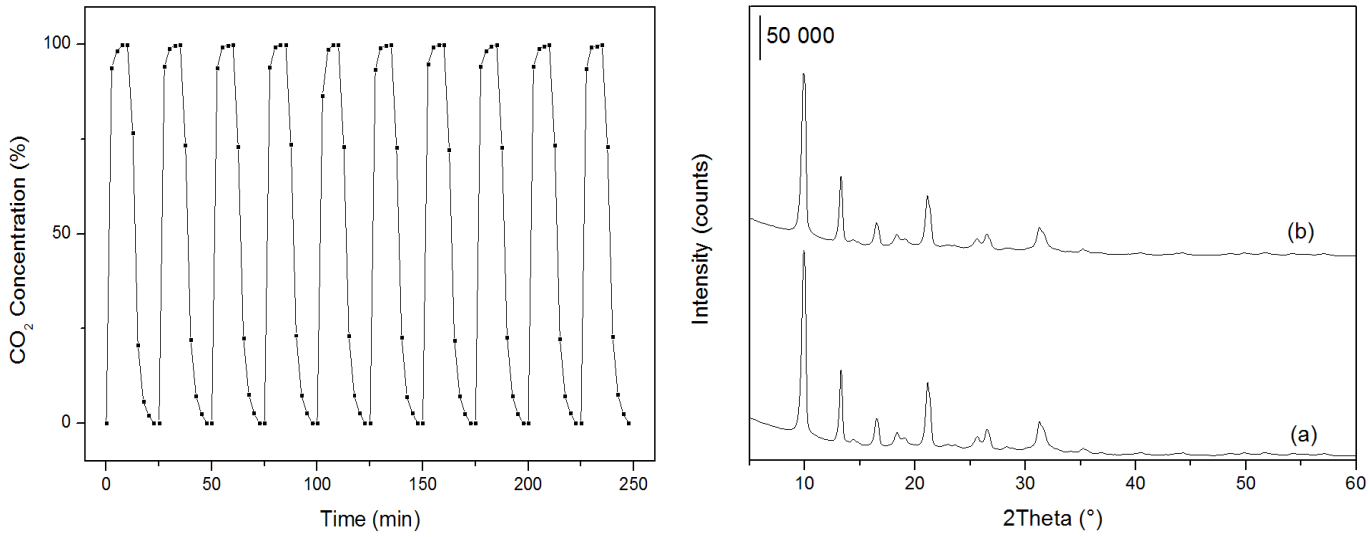

Figure 9. (**A**) CO_2 adsorption/desorption cycling on Na-SSZ-13-meso-0.4 and (**B**) XRD pattern of Na-SSZ-13-meso-0.4-40 (a) before and (b) after 15 sorption cycles.

3. Materials and Methods

3.1. Synthesis of Microporous and Mesoporous SSZ-13

Conventional SSZ-13 was synthesised according to the literature [35]. First, 4 g of 1 M NaOH solution and 4 g of 1 M N,N,N-trimethyl-1-adamantammonium hydroxide (TMAdOH, Sachem Europe B.V., Zaltbommel, The Netherlands, 25%) were mixed in a round-bottomed flask for 15 min, after which 4 g of deionised water was added dropwise. Next, 0.1 g of aluminium hydroxide (Sigma Aldrich, Gillingham, UK) and 4 g of deionised water were added slowly under vigorous stirring. After 30 min, 1.2 g of fumed silica and 4 g of deionised water were added and stirred for 2 h at room temperature to obtain a homogeneous gel with a composition of 10 TMAdOH: 10 Na_2O: 3 $Al(OH)_3$: 100 SiO_2: 4400 H_2O. Then, the gel was transferred to a Teflon-lined stainless-steel autoclave and placed in an oven at 150 °C for 4 days. After this time, the solid was recovered by vacuum filtration (as-synthesized), and it is further calcined at 550 °C at a rate of 2 °C·min^{-1} for 10 h.

Mesoporous SSZ-13 was synthesised using a combination of templates by the dual-templating method. TMAdOH and 3-(trimethoxysilyl)propyl dimethyl octadecyl ammonium chloride (TPOAC) (Sigma Aldrich) are used as the structure-directing agent (SDA) and mesopore-generating (mesopogen) template. The molar composition of the gel was "xTPOAC: 10 TMAdOH: 10 Na_2O: 3 $Al(OH)_3$: 100 SiO_2: 4400 H_2O", where x was 2, 4, 6, or 8. The gel resulting from this synthesis was transferred to a Teflon-lined stainless-steel autoclave and placed in oven at 150 °C for 6 days. After this time, the solid was recovered by vacuum filtration (as-synthesized) and calcined at 550 °C for 10 h.

The proton forms of the materials were obtained by converting the as-synthesised Na-SSZ-13 into their ammonium form via three consecutive ion exchanges with NH_4NO_3. First, 60 mL of 1 M solution was added per gram of as-synthesized solid; then, the solution was heated to 80 °C and stirred for 2 h. After each exchange, the solution was vacuum filtered, and the resulting solid was washed with deionised water. The NH_4-SSZ-13 acquired was dried at 100 °C for 12 h and calcined at 550 °C for 6 h to obtain the proton form of the zeolite.

Microporous SSZ-13 materials are denoted as x-SSZ-13-micro-y or x-SSZ-13-meso-w depending on whether they are conventional microporous zeolites or mesoporous zeolites, where x denotes the cation in the framework, Na^+ or H^+, y is the silicon to aluminium ratio, 20 or 40, and w is the template ratio: 0.2, 0.4, 0.6, or 0.8.

3.2. Characterisation

The crystallinity of solids was measured by powder XRD using a PANalytical X'Pert Pro X-ray diffractometer (Malvern Panalytical, Malvern, UK). The X-ray source was copper with a wavelength of 1.5405 Å. Diffractograms were carried out from 5° to 60° with a step size of 0.067°. BET measurements were carried out using a Micromeritics ASAP 2020 equipment (Micromeritics UK Ltd., Gloucestershire, UK). The t-plot method was used to calculate micropore volume and pore size distribution. Measurements considered a thickness range of 30–40 Å. CO_2 isotherms were obtained using a Quadrasorb SI instrument (Quantachrome, Boynton Beach, FL, USA) at 0 °C in ice bath. The Si/Al ratio content of calcined materials was determined by ICP analysis. Prior to analysis on a Perkin-Elmer Optima 4300, the samples were dissolved in a mixture of concentrated HF and concentrated HNO_3 in water (1:1:1 *v/v/v*). SEM images were obtained using an FEI Quanta FEG–Environmental Scanning Electron Microscope (Fei UK Ltd., Altrincham, UK) whereby samples were mounted on carbon tape for measurements.

3.3. Cycling Experiments

Materials were pressed and pelletised before being sieved to the desired particle size of 250–425 μm. A 50 cm long quartz tube with an inner diameter of 60 mm was used for CO_2 capture adsorption/desorption cycling experiments. In a typical experiment, the material under study with a particle size of 250–425 μm was placed in the quartz tube reactor. A pre-treatment procedure was employed to avoid any impurities present in the material. For that purpose, the material was heated in situ by flowing pure N_2 (99.999%) to the temperature of 350 °C at a rate of 3 °C·min^{-1}. After 30 min at 350 °C, the reactor was cooled to 25 °C and kept at 25 °C for the rest of the experiments. Later, the N_2 flow was stopped, and the CO_2/N_2 mixture flow was passed through the reactor instantaneously using a 4-way valve. The partial pressure of CO_2 was 0.1 atm and the total pressure was 2 atm. The effluent was analysed by the GC-TCD (Model GC-2014, Shimadzu Instruments, Tokyo, Japan) equipped with a Porapak Q column every 2.5 min. When the concentration of the CO_2 at the effluent reached its maximum, the desorption process was started. For this, the CO_2/N_2 mixture flow was stopped, and pure N_2 flow started instantaneously using a 4-way valve. Then, the concentration of CO_2 in the effluent was monitored until no CO_2 was observed. At this stage, the whole process was repeated by starting the adsorption process again. The GC-TCD was operated at an injection temperature of 40 °C and a detector temperature of 100 °C.

4. Conclusions

Microporous and mesoporous high-silica chabazite type zeolites SSZ-13 were synthesized in both their sodium and proton form, and the subsequent materials were tested for CO_2 capture capability. In all cases, mesoporous SSZ-13 exhibited faster sorption kinetics than microporous SSZ-13, but not necessarily a higher CO_2 capacity. The greatest rate of CO_2 adsorption amongst sodium form zeolites was seen in Na-SSZ-13-meso-0.4 with the best performing proton analogue being H-SSZ-13-meso-0.6. H-SSZ-13-meso analogues exhibited good CO_2 capacities and quick sorption cycling leading to the best rates of adsorption among the materials. Na-SSZ-13-meso-0.4, being the best-performing sodium analogue of the samples, was cycled 15 times to assess its recyclability, and it was found that the sorbent is stable in terms of both capacity and crystallinity. It can be concluded from the results obtained that the introduction of a mesopore network in SSZ-13 led to good adsorption/desorption kinetics while maintaining the crystalline properties of the microporous zeolite and hence the CO_2 capture capability. Further study on a larger scale and long-term stability could provide an indication of their potential to capture CO_2 effectively and efficiently in a real-life application.

Author Contributions: Conceptualization, V.D.; methodology, V.D.; software, V.D. and L.H.; validation, V.D. and L.H.; formal analysis, V.D. and L.H.; investigation, V.D. and L.H.; resources, V.D.; data

curation, V.D. and L.H.; writing—original draft preparation, V.D. and L.H.; writing—review and editing, V.D.; visualization, V.D. and L.H.; supervision, V.D.; project administration, V.D.; funding acquisition, V.D. All authors have read and agreed to the published version of the manuscript.

Funding: This research was funded by The Royal Society, Research Grant, grant number RG120620 and the UK Engineering and Physical Sciences Research Council (EPSRC) (grant EP/P511432/1 Global Challenge Research Fund (GCRF) Institutional Award for the University of Warwick).

Data Availability Statement: The data supporting this article are available at http://wrap.warwick.ac.uk/160127 (accessed on 11 November 2021).

Acknowledgments: We thank to Javier Fernández in his assistance with surface area measurements.

Conflicts of Interest: The authors declare no conflict of interest. The funders had no role in the design of the study; in the collection, analyses, or interpretation of data; in the writing of the manuscript, or in the decision to publish the results.

References

1. Martins, F.; Felgueiras, C.; Smitkova, M.; Caetano, N. Analysis of Fossil Fuel Energy Consumption and Environmental Impacts in European Countries. *Energies* **2019**, *12*, 964. [CrossRef]
2. Ram, M.; Child, M.; Aghahosseini, A.; Bogdanov, D.; Lohrmann, A.; Breyer, C. A comparative analysis of electricity generation costs from renewable, fossil fuel and nuclear sources in G20 countries for the period 2015–2030. *J. Clean. Prod.* **2018**, *199*, 687–704. [CrossRef]
3. Wang, Y.; Zhao, L.; Otto, A.; Robinius, M.; Stolten, D. A Review of Post-combustion CO_2 Capture Technologies from Coal-fired Power Plants. *Energy Proced.* **2017**, *114*, 650–665. [CrossRef]
4. Casco, M.E.; Martínez-Escandell, M.; Silvestre-Albero, J.; Rodríguez-Reinoso, F. Effect of the porous structure in carbon materials for CO_2 capture at atmospheric and high-pressure. *Carbon* **2014**, *67*, 230–235. [CrossRef]
5. García, S.; Gil, M.V.; Martín, C.F.; Pis, J.J.; Rubiera, F.; Pevida, C. Breakthrough adsorption study of a commercial activated carbon for pre-combustion CO_2 capture. *Chem. Eng. J.* **2011**, *171*, 549–556. [CrossRef]
6. Wang, J.; Pu, Q.; Ning, P.; Lu, S. Activated carbon-based composites for capturing CO_2: A review. *Greenh. Gases.* **2021**, *11*, 377–393. [CrossRef]
7. Younas, M.; Rezakazemi, M.; Daud, M.; Wazir, M.B.; Ahmad, S.; Ullah, N.; Inamuddin; Ramakrishna, S. Recent progress and remaining challenges in post-combustion CO_2 capture using metal-organic frameworks (MOFs). *Prog. Energy Combust. Sci.* **2020**, *80*, 100849. [CrossRef]
8. Hu, Z.; Wang, Y.; Shah, B.B.; Zhao, D. CO_2 Capture in Metal–Organic Framework Adsorbents: An Engineering Perspective. *Adv. Sustain. Syst.* **2019**, *3*, 1800080. [CrossRef]
9. Wang, J.; Huang, L.; Yang, R.; Zhang, Z.; Wu, J.; Gao, Y.; Wang, Q.; O'Hare, D.; Zhong, Z. Recent advances in solid sorbents for CO_2 capture and new development trends. *Energ. Environ. Sci.* **2014**, *7*, 3478–3518. [CrossRef]
10. D'Alessandro, D.M.; Smit, B.; Long, J.R. Carbon Dioxide Capture: Prospects for New Materials. *Angew. Chem. Int. Ed.* **2010**, *49*, 6058–6082. [CrossRef] [PubMed]
11. Raganati, F.; Miccio, F.; Ammendola, P. Adsorption of Carbon Dioxide for Post-combustion Capture: A Review. *Energy Fuel* **2021**, *35*, 12845–12868. [CrossRef]
12. Ammendola, P.; Raganati, F.; Chirone, R.; Miccio, F. Fixed bed adsorption as affected by thermodynamics and kinetics: Yellow tuff for CO_2 capture. *Powder Technol.* **2020**, *373*, 446–458. [CrossRef]
13. Dhoke, C.; Zaabout, A.; Cloete, S.; Amini, S. Review on Reactor Configurations for Adsorption-Based CO_2 Capture. *Ind. Eng. Chem. Res.* **2021**, *60*, 3779–3798. [CrossRef]
14. Dhoke, C.; Cloete, S.; Krishnamurthy, S.; Seo, H.; Luz, I.; Soukri, M.; Park, Y.-k.; Blom, R.; Amini, S.; Zaabout, A. Sorbents screening for post-combustion CO_2 capture via combined temperature and pressure swing adsorption. *Chem. Eng. J.* **2020**, *380*, 122201. [CrossRef]
15. Yang, J.; Zhao, Q.; Xu, H.; Li, L.; Dong, J.; Li, J. Adsorption of CO_2, CH_4, and N_2 on Gas Diameter Grade Ion-Exchange Small Pore Zeolites. *J. Chem. Eng. Data* **2012**, *57*, 3701–3709. [CrossRef]
16. Merel, J.; Clausse, M.; Meunier, F. Experimental Investigation on CO_2 Post-Combustion Capture by Indirect Thermal Swing Adsorption Using 13X and 5A Zeolites. *Ind. Eng. Chem. Res.* **2008**, *47*, 209–215. [CrossRef]
17. Pham, T.D.; Liu, Q.; Lobo, R.F. Carbon dioxide and nitrogen adsorption on cation-exchanged SSZ-13 zeolites. *Langmuir* **2013**, *29*, 832–839. [CrossRef]
18. Zhang, J.; Singh, R.; Webley, P.A. Alkali and alkaline-earth cation exchanged chabazite zeolites for adsorption based CO_2 capture. *Micropor. Mesopor. Mat.* **2008**, *111*, 478–487. [CrossRef]
19. Hudson, M.R.; Queen, W.L.; Mason, J.A.; Fickel, D.W.; Lobo, R.F.; Brown, C.M. Unconventional, Highly Selective CO_2 Adsorption in Zeolite SSZ-13. *J. Am. Chem. Soc.* **2012**, *134*, 1970–1973. [CrossRef] [PubMed]
20. Bezerra, D.P.; da Silva, F.W.M.; de Moura, P.A.S.; Sousa, A.G.S.; Vieira, R.S.; Rodriguez-Castellon, E.; Azevedo, D.C.S. CO_2 adsorption in amine-grafted zeolite 13X. *Appl. Surf. Sci.* **2014**, *314*, 314–321. [CrossRef]

21. Kamimura, Y.; Shimomura, M.; Endo, A. CO_2 adsorption–desorption properties of zeolite beta prepared from OSDA-free synthesis. *Micropor. Mesopor. Mat.* **2016**, *219*, 125–133. [CrossRef]
22. Abanades, J.C.; Arias, B.; Lyngfelt, A.; Mattisson, T.; Wiley, D.E.; Li, H.; Ho, M.T.; Mangano, E.; Brandani, S. Emerging CO_2 capture systems. *Int. J. Green Energy* **2015**, *40*, 126–166. [CrossRef]
23. Hillen, L.; Degirmenci, V. Synthesis Methods for the Production of Hierarchically Mesoporous and Microporous Zeolites. *Rev. Adv. Sci. Eng.* **2015**, *4*, 147–162. [CrossRef]
24. Koekkoek, A.J.J.; Degirmenci, V.; Hensen, E.J.M. Dry gel conversion of organosilane templated mesoporous silica: From amorphous to crystalline catalysts for benzene oxidation. *J. Mater. Chem.* **2011**, *21*, 9279–9289. [CrossRef]
25. Degirmenci, V.; Hensen, E.J.M. Development of a Heterogeneous Catalyst for Lignocellulosic Biomass Conversion: Glucose Dehydration by Metal Chlorides in a Silica-Supported Ionic Liquid Layer. *Environ. Prog. Sustain. Energy* **2014**, *33*, 657–662. [CrossRef]
26. Koekkoek, A.J.J.; Tempelman, C.H.L.; Degirmenci, V.; Guo, M.; Feng, Z.; Li, C.; Hensen, E.J.M. Hierarchical zeolites prepared by organosilane templating: A study of the synthesis mechanism and catalytic activity. *Catal. Today* **2011**, *168*, 96–111. [CrossRef]
27. Choi, M.; Na, K.; Kim, J.; Sakamoto, Y.; Terasaki, O.; Ryoo, R. Stable single-unit-cell nanosheets of zeolite MFI as active and long-lived catalysts. *Nature* **2009**, *461*, 246–249. [CrossRef]
28. Choi, M.; Cho, H.S.; Srivastava, R.; Venkatesan, C.; Choi, D.H.; Ryoo, R. Amphiphilic organosilane-directed synthesis of crystalline zeolite with tunable mesoporosity. *Nat. Mater.* **2006**, *5*, 718–723. [CrossRef]
29. Chen, C.; Ahn, W.-S. CO_2 adsorption on LTA zeolites: Effect of mesoporosity. *Appl. Surf. Sci.* **2014**, *311*, 107–109. [CrossRef]
30. Wu, L.; Degirmenci, V.; Magusin, P.C.M.M.; Lousberg, N.J.H.G.M.; Hensen, E.J.M. Mesoporous SSZ-13 zeolite prepared by a dual-template method with improved performance in the methanol-to-olefins reaction. *J. Catal.* **2013**, *298*, 27–40. [CrossRef]
31. Wu, L.; Degirmenci, V.; Magusin, P.C.M.M.; Szyja, B.M.; Hensen, E.J.M. Dual template synthesis of a highly mesoporous SSZ-13 zeolite with improved stability in the methanol-to-olefins reaction. *Chem. Commun.* **2012**, *48*, 9492–9494. [CrossRef] [PubMed]
32. Samanta, A.; Zhao, A.; Shimizu, G.K.H.; Sarkar, P.; Gupta, R. Post-Combustion CO_2 Capture Using Solid Sorbents: A Review. *Ind. Eng. Chem. Res.* **2012**, *51*, 1438–1463. [CrossRef]
33. Sjostrom, S.; Krutka, H. Evaluation of solid sorbents as a retrofit technology for CO_2 capture. *Fuel* **2010**, *89*, 1298–1306. [CrossRef]
34. Younas, M.; Sohail, M.; Leong, L.K.; Bashir, M.J.; Sumathi, S. Feasibility of CO_2 adsorption by solid adsorbents: A review on low-temperature systems. *Int. J. Environ. Sci. Technol.* **2016**, *13*, 1839–1860. [CrossRef]
35. Zones, S.I.; Hwang, S.-J.; Davis, M.E. Studies of the Synthesis of SSZ-25 Zeolite in a "Mixed-Template" System. *Chem. Eur. J.* **2001**, *7*, 1990–2001. [CrossRef]